Interaction between multiple bubbles in microchannel flow boiling and the effects on heat transfer

L Lombaard[a], M A Moghimi[a,c], P Valluri[b], J P Meyer[a]

[a] Department of Mechanical and Aeronautical Engineering, University of Pretoria, Pretoria, South Africa

[b] Institute for Multiscale Thermofluids, School of Engineering, The University of Edinburgh, Edinburgh, United Kingdom

[c] Department of Engineering, Staffordshire University, Stoke-On-Trent, United Kingdom.
Email address: Mohammad.Moghimi-Ardekani@staffs.ac.uk

Abstract Flow boiling in microchannels have widely been studied in order to design more efficient cooling systems with numerical simulations forming a crucial part to deal with the areas that cannot be investigated experimentally. Previously published research largely focussed on the behaviour of a single bubble. Here, we focus on the behaviour of multiple bubbles. In this study, the influence of the distance between the bubbles (liquid slug length) is investigated in both an axisymmetric and a planar domain for two and three bubbles present. In this regard, an interface-tracking adaptive mesh refinement model was implemented to improve simulation time. Results show that the heat transfer was improved with sequential bubbles, and a 50% increase in heat transfer coefficient was observed for the cases investigated with three bubbles present. The heat transfer also improved the closer the bubbles were together.

Keywords: *Flow boiling; Microchannel Multiple bubbles; Computational Fluid Dynamics*

1. Introduction

With the reduction of electronics came the need for higher heat dissipation, which is beyond the capabilities of single-phase cooling [1, 2]. This has led to the development of two-phase flow-cooling systems. Examples of these cooling systems are microchannel heat sinks, which were investigated in this research, and jet-impingement cooling. Microchannel heat sinks provide high heat transfer rates in a compact size. Microchannels also provide better heat transfer than their conventional counterparts do due to a larger liquid-vapour interface area per unit volume [3].

Fully developed single-phase flow is limited to conduction heat transfer [4]. The flow can be disturbed to become more turbulent to improve the heat transfer of a single-phase system. This can be achieved through either the geometry of the channel [5, 6] or through alternating fluid properties. Alternating fluid properties can be achieved with solid particles for nanofluids, immiscible droplets or gas bubbles. Gas bubbles can be added from an external source or by boiling the liquid.

Boiling heat transfer can be divided into pool boiling and flow boiling. Pool boiling occurs in the absence of bulk fluid motion and is most effective in the nucleate boiling regime. The nucleate boiling regimes provides the highest heat flux for the lowest surface temperature [7]. Flow boiling occurs when bulk fluid motion is present and can be classified as external flow boiling or internal flow boiling, also referred to as two-phase flow. Two-phase flow has a significantly higher heat transfer coefficient (HTC) than that of pool boiling due to additional convection heat transfer [8].

The advantage of two-phase flow over single-phase flow is that the latent heat of the fluid is used with the sensible heat [9]. There are different regimes in internal flow boiling, namely bubbly flow, slug flow, churn flow, film flow and annular flow [10]. Bubbly flow occurs as bubbles form and detach from the heated surface. These bubbles are discrete and are smaller than the hydraulic diameter of the channel [11]. As the bubbles grow and coalesce, the flow develops into slug flow.

Slug flow is especially of interest due to its high heat transfer characteristics [12]. This flow regime is characterised by alternating liquid and vapour slugs, with a thin liquid film between the wall and vapour slug or bubble [13]. The liquid film is important because it is where the highest heat transfer occurs [14]. Another important aspect of slug flow is the presence of recirculating zones in the slugs, as shown in Figure 1. These recirculation zones transport cooler fluid from the centre to the wall, replacing the heated fluid and improving heat transfer [15]. From slug flow, the flow develops further into churn flow, and finally, into film and annular flow.

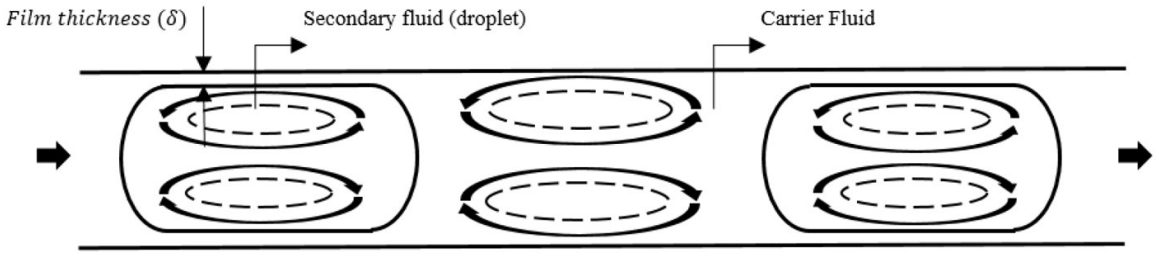

Although flow boiling is employed in practice and the overall effects are understood, still the finer mechanics involved are not understood, such as the interactions between bubbles. This is due to the small scales involved and the limitations of experimental hardware [16]. These limitations are not relevant when using computational fluid dynamics (CFD) to investigate the phenomena. It should be noted that CFD simulations also have constraints, and therefore, it is necessary to consider the set-

up of the model to ensure a feasible study. One of the major limitations is the mesh density. The number of mesh elements is directly proportional to the computational time and resources required.

To ensure that the CFD simulation produces accurate results, the mesh needs to be fine enough to capture high gradients of thermofluid properties. An example of this is the liquid-vapour interface between the bubble and the liquid. This led researchers to use a very fine uniform mesh when investigating microscale slug flow. However, using a fine mesh increases the computational cost and making three-dimensional or more complex simulations nearly impossible. Due to these limitations, most research is conducted on a two-dimensional domain and with a single vapour bubble at the start of the simulation. One of the studies that did investigate multiple bubbles was conducted by Magnini et al. [9]. They investigated the effect of two bubbles on the heat transfer coefficient (HTC) for a single case. More recently, Magnini and Thome [3] did an in-depth study. They patched new bubbles into the domain near the entrance at various frequencies and adjusted the mass flux and heat flux for different scenarios.

Recent progress in the techniques used has made it possible to investigate larger domains. One example is adaptive meshing. Adaptive meshing improves computational cost by reducing the number of mesh elements but maintaining accuracy. This is accomplished by using a coarse mesh in the bulk of the domain and refined cells in the regions where high gradients are present.

This research aims to evaluate the effect of different liquid slug lengths or initial spacings between vapour bubbles in microchannel slug flow. To start, a short description of the domain design and governing equations is given, followed by a layout of the proposed solvers and methods used. The set-up is then compared with previous cases reported in the literature. Lastly, several simulations conducted with different initial spacings to review the effect on heat transfer are presented.

2. Numerical methodology

2.1 Computational domain

This study investigated the interaction between multiple bubbles in a microchannel. The working fluids were the liquid and vapour phases of refrigerant R245fa and these are assumed to be incompressible, immiscible, viscous and Newtonian, flowing within a two-dimensional laminar microchannel. Two different domains were used in the study: an axisymmetric domain and a planar domain. Both of the domains had a height of D = 0.5 mm and a length of 72D. The domains were divided into three regions: an adiabatic region at the inlet and the outlet, with a heated section in the middle. The entrance region was 16D, the exit region was 34D and the heated section was 22D in length, as shown in Figure 2. This was chosen to mimic the numerical investigation of Magnini et al. [9] . Two pill-shaped bubbles were patched into the domain in the adiabatic entrance region. Saturated fluid entered the inlet at a temperature of 304.15 K and a mass flux of 550 kg/m^2.s. The outlet had a zero-gauge pressure condition applied, while the heated walls had a heat flux of 5 kW/m^2 and a no-slip condition applied. The initial location (x_i) of the front bubble was 3.5D from the start of the heated section. The bubbles initially had an approximate length (L_{Bi}) of 3D and the initial distance between the bubbles was varied (L_{int}).

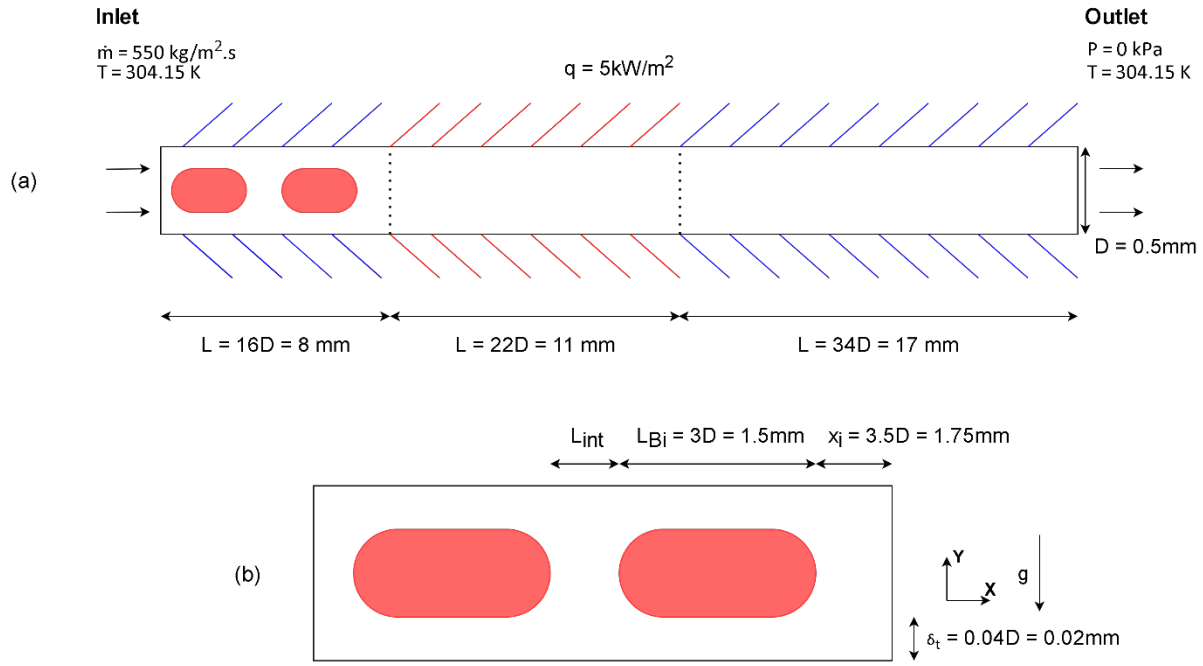

Figure 2: Bubble locations and boundary conditions with (a) illustrating the full domain and (b) the inlet region (not to scale)

Table 1: Properties of refrigerant R245fa (adapted from Ferrari et al. [12])

Property	Liquid	Vapour
Density [kg/m^3]	1322	10.5
Viscosity [µPa.s]	375.4	10.5
Specific heat [J/kg.K]	1352	926
Conductivity [mW/m.K]	88.2	14.4
Saturation temperature [K]	304.15	
Surface tension [mN/m]	13.3	
Latent heat capacity [kJ/kg]	187.3	

For this study, the volume of fluid (VOF) method was used. With the VOF method, the domain was represented as a single fluid and the volume fraction, α, was used to distinguish between liquid and vapour. The volume fraction had a value of 1 in the pure liquid region and 0 in the pure vapour region. At the interface between the phases, the volume fraction was smeared over three or four cells and changed from 0 to 1. The volume fraction and the properties of the two phases (listed in Table 1) were used to calculate the values of the single-fluid properties, e.g. density and viscosity, with the following equation:

$$\emptyset = \emptyset_L \alpha + (1 - \alpha)\emptyset_v \quad (1)$$

where $\emptyset$ denotes any scalar property and the subscripts L and v indicate the liquid and vapour properties respectively.

2.2 Governing equations

For each iteration of the simulation, a complete set of governing equations are solved including conservation of mass, momentum and energy, scalar transport and volume fraction advection. The equations are listed below:

$$\nabla(\tilde{u}) = 0 \quad (2)$$

$$\rho\left(\frac{\partial\tilde{u}}{\partial\tilde{t}} + \tilde{u}\cdot\tilde{\nabla}\tilde{u}\right) = -\tilde{\nabla}P + \mu\tilde{\nabla}^2\tilde{u} + \sigma\tilde{\kappa}\tilde{n}\delta \quad (3)$$

$$\rho c_p\left(\frac{\partial T}{\partial t} + \tilde{u}\cdot\tilde{\nabla}T\right) = \bar{k}\tilde{\nabla}^2T + \tilde{\nabla}h_{fg}\dot{m} \quad (4)$$

$$\frac{\partial\emptyset}{\partial t} + \nabla\cdot\emptyset\tilde{u} = \emptyset\nabla\cdot\emptyset \quad (5)$$

$$\frac{1}{\rho}\left[\frac{\partial}{\partial t}(c\rho) + \nabla\cdot(c\rho\tilde{u})\right] = \frac{1}{\rho}[S_c + S_{mV} - S_{mL}] \quad (6)$$

where ρ is the density [kg/m^3], u is the velocity [m/s], P is the pressure [kPa], T is the temperature [K], σ is the surface tension coefficient [mN/m], μ is the viscosity [µPa.s], h_{fg} is the latent heat capacity [kJ/kg], $\dot{m}$ is the volumetric mass transfer rate [kg/m^3.s] and S is a volumetric source term.

2.3 Flow solver

A number of different methods were necessary to solve the flow equations during each time step. The following settings and solvers were used in the study:

- A pressure-based solver was used; and to calculate the pressure, the PRESTO! (PREssure STaggered Option) was used.
- For pressure-velocity coupling, the PISO (Pressure-Implicit with Splitting of Operators) method was selected.
- Gradients for the momentum and energy equations were calculated with a second-order upwind method.
- For the volume fraction, a second-order implicit method was used.
- The interface was propagated and reconstructed with a compressive scheme. This scheme recreates the interface by using the cell values and unit normal related to the cell and its surroundings.

For time advancement, an implicit first-order time-stepping method was utilised. The time advancement was iterative and solved the flow and other scalar equations simultaneously until their residuals had converged below 1e-6. The time step was calculated with the Courant-Friedrichs Lewy number (CFL) by using the following equation [17]:

$$CFL = \frac{u\Delta t}{\Delta x} \quad (7)$$

A maximum CFL = 0.25 was used. This ensured that the information did not travel further than the characteristic length of the mesh elements and kept the simulation stable. To prevent no more than 1% of the liquid evaporating from each cell during a time step, an additional limitation of $\Delta t_{max} < 1\times10^{-6}s$ was applied, resulting in time steps ranging from $2\times10^{-7} - 1\times10^{-6}s$ for the simulations.

2.4 Solution initialisation and UDF

A steady-state case was run to obtain fully developed velocity, pressure and temperature profiles within the simulation domain, using only liquid R245fa. After the profiles were developed, the simulation was changed to transient mode. Multiple vapour slugs were then patched into the adiabatic inlet region and the mesh elements at the interface were refined. The properties were set to those at saturation temperature and uniform profiles for temperature, pressure and velocity were implemented.

Once the bubbles were patched and the liquid-vapour interface was defined, a user-defined function (UDF) was employed to calculate the mass transfer and implement mesh adaption. The UDF was developed by Potgieter [18] and was used to assist in calculating mass transfer in the microscale and ensuring that mass transfer only occurred at the interface. The mass transfer model that was used in the UDF is the simplified version of the Schrage model by Tanasawa [19]:

$$\dot{m} = \frac{2\omega}{2-\omega}\sqrt{\frac{M}{2\pi R}}\left[\frac{\rho_g h_L (T - T_{sat})}{T_{sat}^{3/2}}\right] \tag{8}$$

where $\dot{m}$ is the mass transfer rate (kg/m^3.s), M is the molecular mass (kg/mol), R is the gas constant and $\omega = 1$. It was assumed that the saturation temperatures for the liquid and vapour phase were equal (T_{sat}).

3. Verification and validation

This study aimed to build on the research of Potgieter [18] by investigating the effects of multiple bubbles in a microchannel. Previously, Vermaak et al. [20] using an identical domain found a good correlation between experimental and numerical results. Therefore, in this study, a domain with exactly the same mesh settings (bulk size of 25 µm) but with a longer length is used. Given the adequate mesh refinement tests presented in Vermaak et al. [20] and convergence of results with experimental studies, a separate mesh independence test was not conducted.

To validate the results of this study, these results were compared with previously published research that was conducted in the same simulation domain and with the same working fluid. The average Nusselt number (Nu) in an axisymmetric domain was compared. The Nu was calculated with the following equation:

$$Nu = \frac{hD}{k} \tag{9}$$

where k is the conductivity [W/m.K] and h is the HTC, which was calculated as follows:

$$h = \frac{q}{T_{nw} - T_{sat}} \tag{10}$$

with q as the heat flux [W/m^2], T_{nw} is the near-wall temperature [K] and T_{sat} is the saturation temperature [K].

The Nu was measured along the length of the bubble plus half a liquid slug length in front and behind the bubble. It was averaged by dividing the sum of values along this length by the number of data points. The averaged Nu was plotted against the midpoint position of the bubble, which was measured from the start of the heated section.

The average Nu showed a good agreement with the results published by Magnini et al. [9]. At the leading bubbles, our prediction $14 \geq Nu \geq 9$ is nearly identical to that of Magnini et al. [9] (Figure 3a). The values for the trailing bubbles differed slightly (Figure 3b) with Magnini et al. [9] showing $17 \geq Nu \geq 13$, and our study predicting $16 \geq Nu \geq 11$. We are encouraged by these results and thus, the solver settings were judged to provide accurate results.

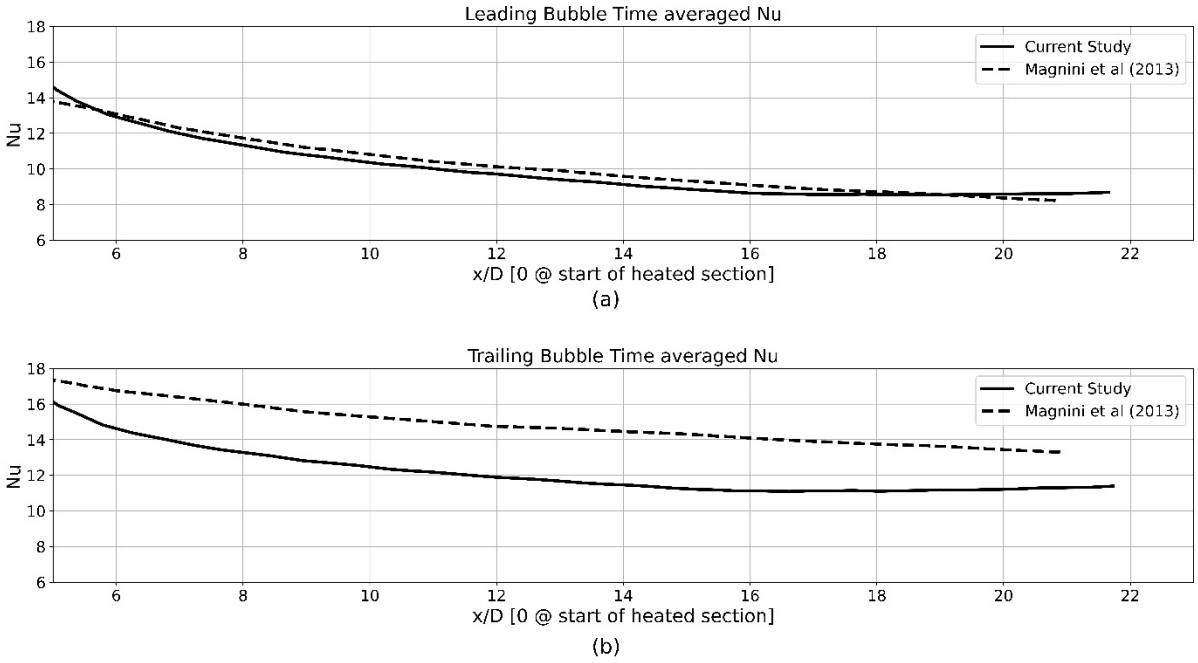

Figure 3: Averaged Nu compared with Magnini et al. [9] *for (a) the leading bubble and (b) the trailing bubble.*

4. Results

During this study, two different scenarios were investigated; one with two bubbles present and the second with three bubbles present. For the two-bubble scenario, both axisymmetric and planar domains were investigated, while only a planar domain was used for the three-bubble scenario. The results discussed in this section were non-dimensionalised.

Lengths were scaled by the diameter (height) of the domain:

$$L' = \frac{L}{D} \quad or \quad L' = \frac{x}{D} \tag{11}$$

Time was scaled as:

$$\tau = \frac{tG}{\rho_L D} \tag{12}$$

where G is the mass flux at the inlet.

4.1 Two-bubble cases

For the axisymmetric cases, the initial distances (L_{int}) investigated were 1D, 3D, 4D, 5D and 6D. With the planar cases, there were additional cases for L_{int} = 0.25D and 0.5D.

All the bubbles had an initial length of 3D (see Figure 2). As the bubbles entered the heated section of the domain, phase change became present and the bubbles started to grow. With the axisymmetric cases, the leading bubbles reached a final length of 13-14D (Figure 4a) and the trailing bubbles 11-12D (Figure 5). The rates of growth differed between the cases, but the final lengths were almost similar. Around τ = 30, there was a jump in the length of the leading bubble for the case of L_{int} = 1D. This happened because the bubbles coalesced. Figure 4b illustrates the merging bubbles,

which correspond to the shaded region in Figure 4a. The coalescences of the bubbles is are also the reason why the L_{int} = 1D graph stops, as shown in Figure 5.

The distance between the bubbles decreased for all the cases (Figure 6). The rate at which the distance decreased was not constant, and the final distances were reduced by 1.5D for the cases of L_{int} = 4-6D. The case for L_{int} = 3D had a reduction of 2D, and for the L_{int} = 1D case, it was reduced to 0.

The fluctuating behaviour of the length and distance shown in the graphs was due to the oscillating nature of the bubble tails. The tails of the bubbles constantly changed between concave and convex in shape. This behaviour is shown in Figure 6b for 5 different time steps, and the corresponding instances are marked in Figure 6a.

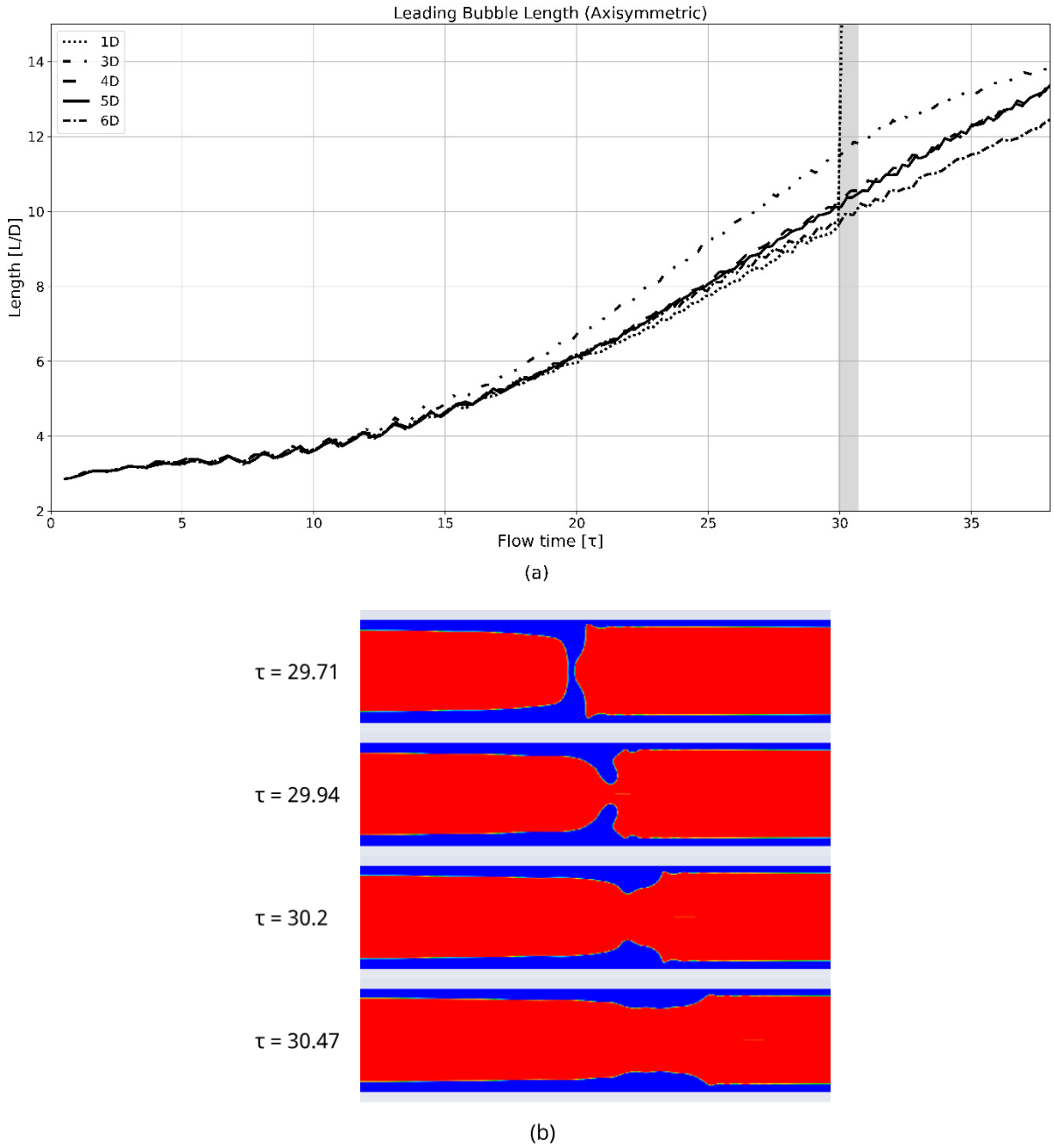

Figure 4: (a) Leading bubble length versus time, for axisymmetric cases, and (b) illustration of the merging bubbles for the case of L_{int} = 1D occurring in the shaded region of (a).

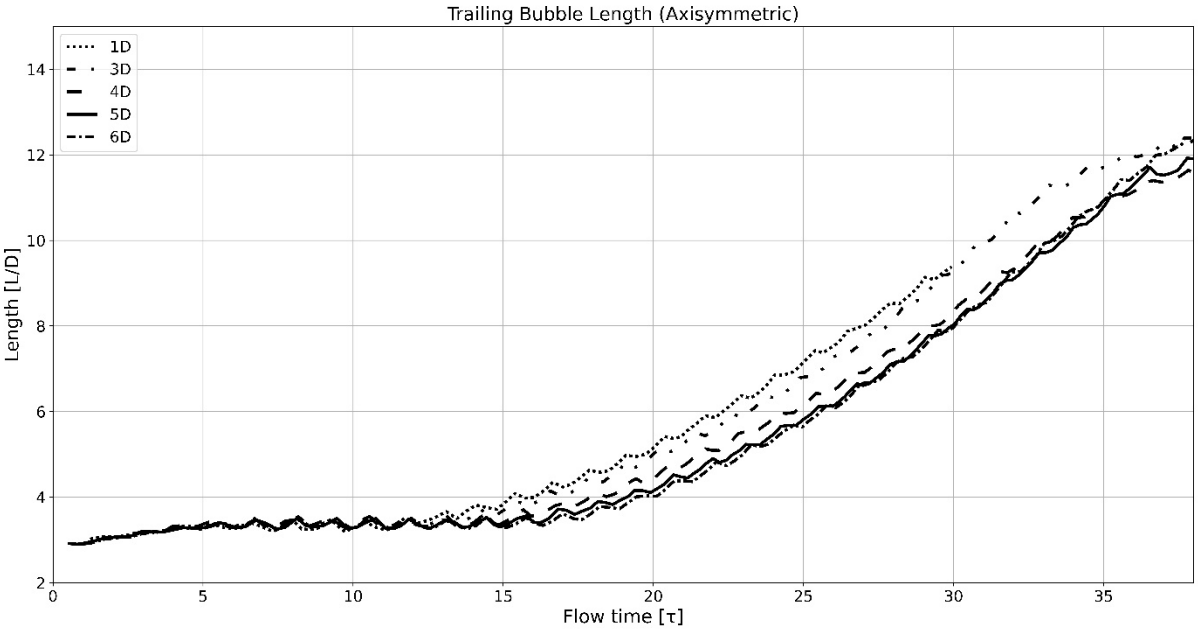

Figure 5: Trailing bubble length versus time, for axisymmetric cases.

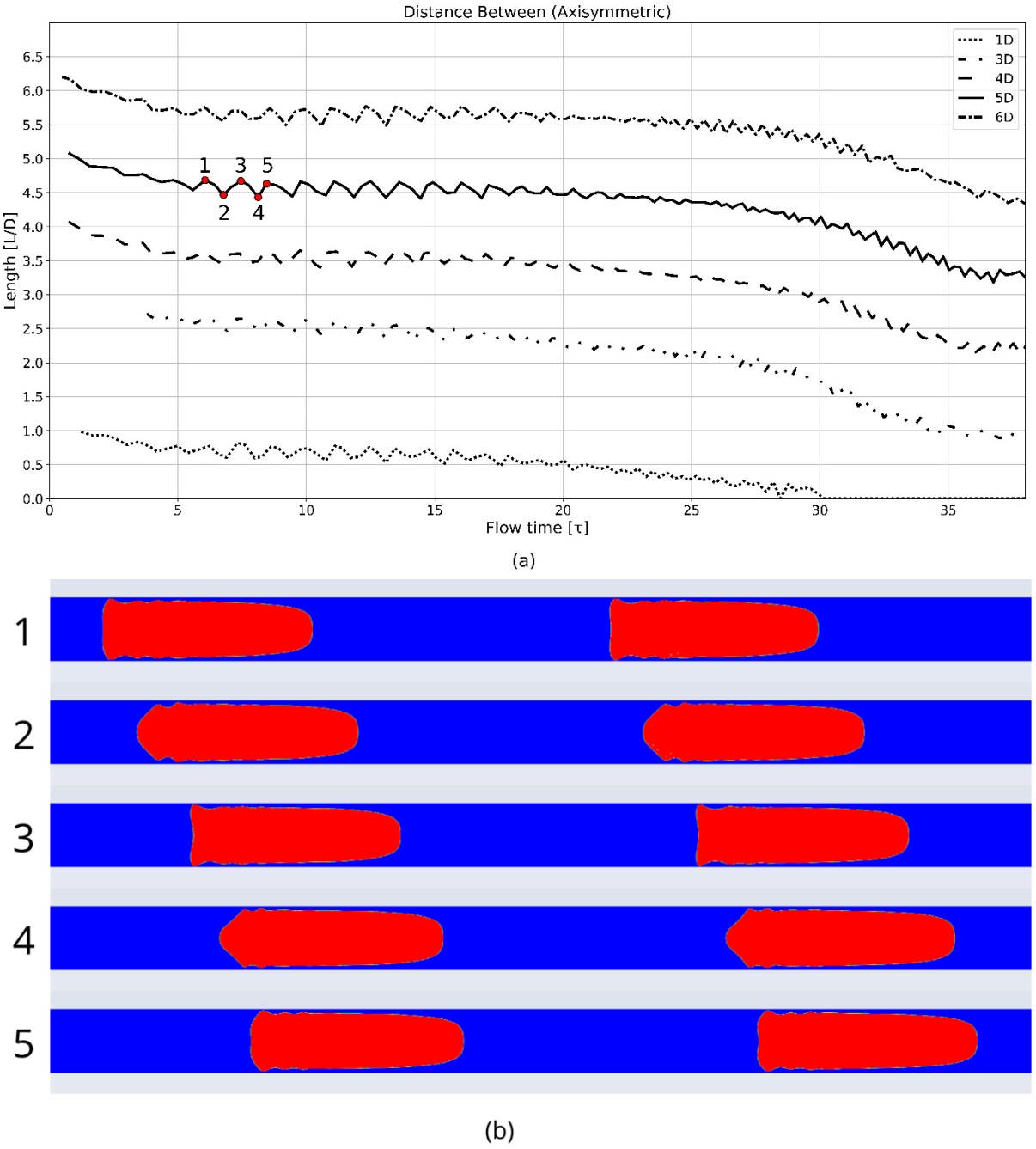

Figure 6: (a) Distance between bubbles versus time, for axisymmetric cases, and (b) illustration of fluctuating bubble tails at corresponding points marked on (a).

When investigating the planar cases, it should be noted that they can be divided into two groups: the first group with initial spacings of more than 1D and the second group with spacings equal or smaller than 1D. There was no significant difference for the leading bubbles (Figure 7), with final lengths ranging between 5.5 and 6.5D. The opposite is true for the trailing bubbles (Figure 8). There, the first group initially had a faster growth rate until 16ms or $\tau = 13$. After that, the second group surpassed the first group. The final length also differed significantly, with the second group ranging between 5.5 and 6.2D compared with the first group in the range of 4.5 and 5D. The difference at the start corresponds to the initial reduction in the distance between the bubbles (Figure 10).

Because there was no heat flux present in this section of the domain, no net evaporation could be present, and this change could only be due to the expansion of the vapour bubble. This expansion continued until an equilibrium state was achieved between the pressure of the phases and the surface tension. After equilibrium was reached, the length remained constant until heat transfer was present. Figure 9 illustrates the difference in length for the cases of L_{int} = 0.25D and L_{int} = 6D at τ = 7.8. As shown, not only was the 6D bubble longer, but the nose also had a sharper profile. The bubble for L_{int} = 0.25D was more confined and had less space to develop.

As for the distance between the bubbles, there was no significant change with time (Figure 10). The first group experienced a reduction corresponding to the initial expansion of the bubble; after which the gradient increased and flattened out. An overall reduction of less than 0.5D is observed. While an increase is observed in the initial spacing of the second group, the increase was less than 0.5D for the L_{int} = 1D case and larger than 0.5D for the other two smaller cases.

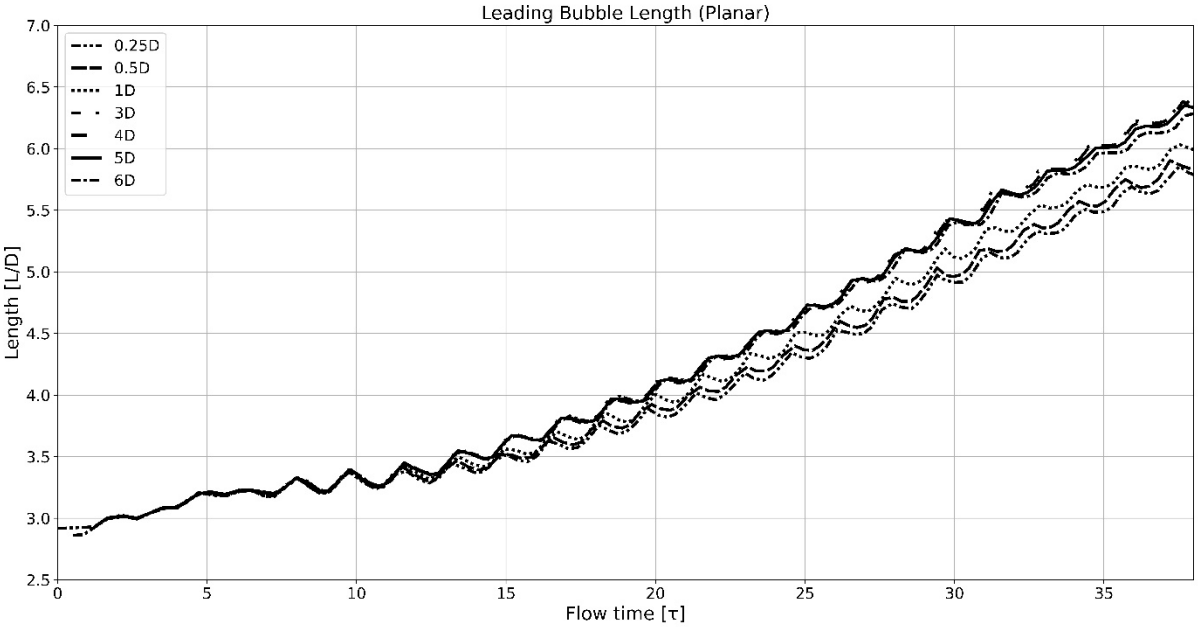

Figure 7: Leading bubble length versus time, for planar cases.

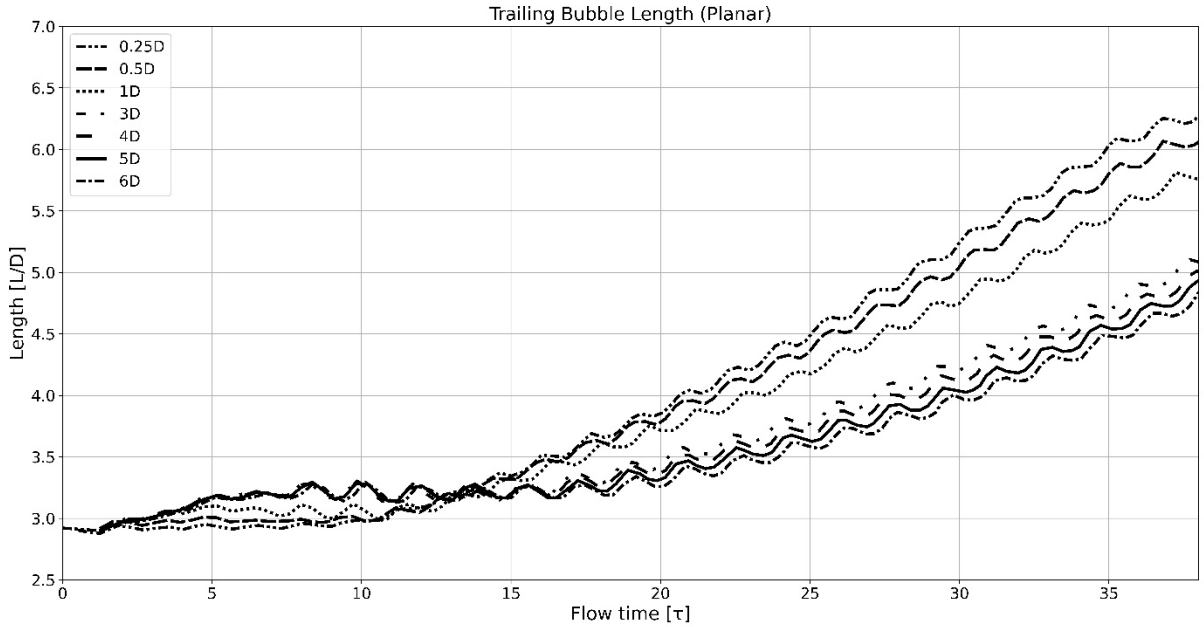

Figure 8: Trailing bubble length versus time, for planar cases.

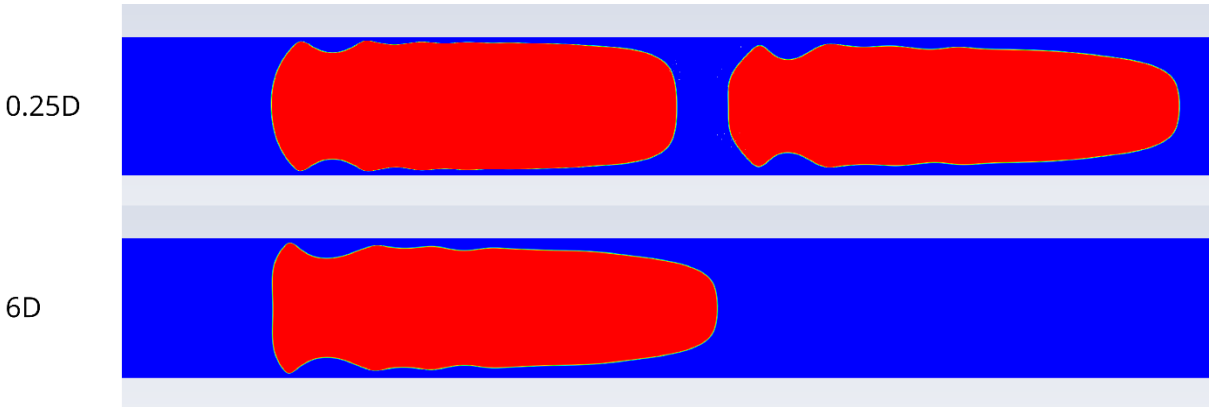

Figure 9: Trailing bubbles for Lint = 0.25D and Lint = 6D at τ = 7.8.

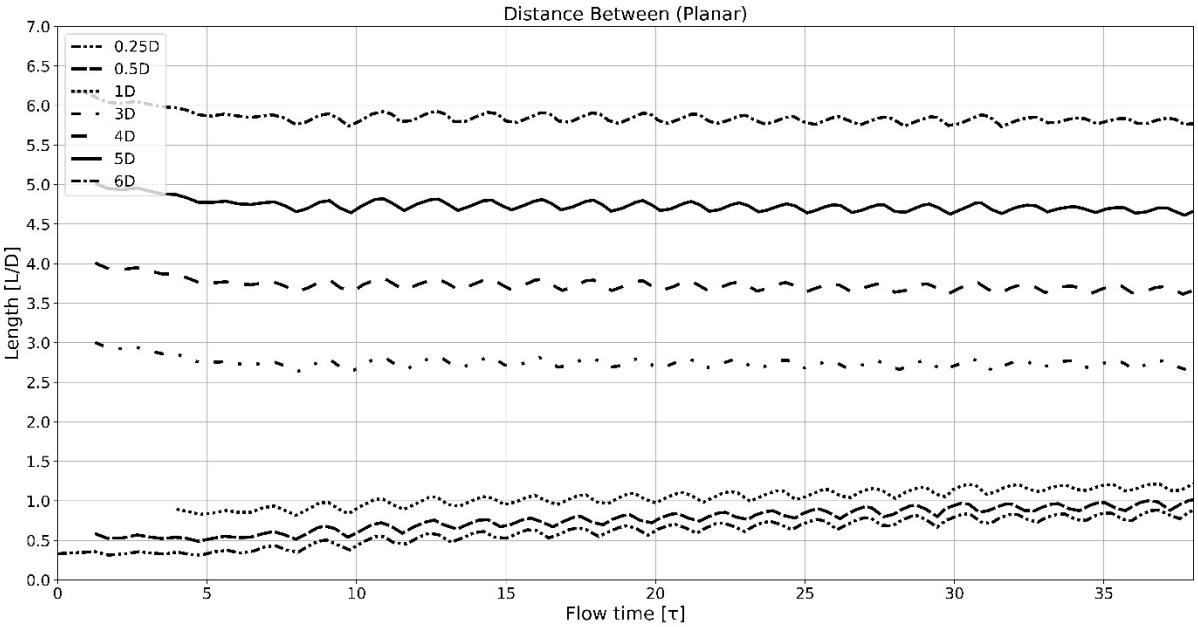

Figure 10: Distance between bubbles, for planar cases.

The Nu for the leading bubbles was similar for all the initial spacings (Figure 11 and Figure 12). In both scenarios, the Nu followed a correlation in the order of:

$$Nu = 25.5x_H^{-0.4} \tag{13}$$

The values initially started high and decreased to around 8. The Nu for the trailing bubbles also fell within a small range of each other, never differing by more than 2 (Figure 13 and Figure 14). The trailing bubbles had a final Nu of between 10 and 12. This suggests that the convection heat transfer was improved from the leading to the trailing bubble. The cases with a larger L_{int} seemed to have a slightly larger Nu, but it was also measured over a longer length because the liquid slug was longer.

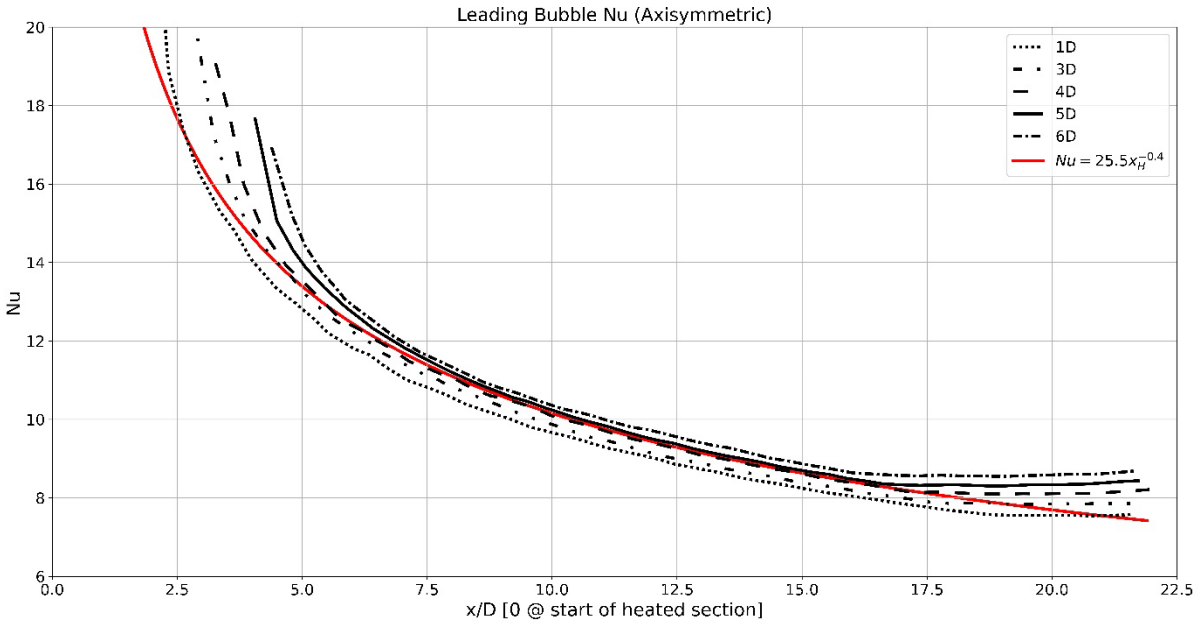

Figure 11: Averaged Nusselt number (Nu) for the leading bubble versus the position of the bubble midpoint, for axisymmetric

cases.

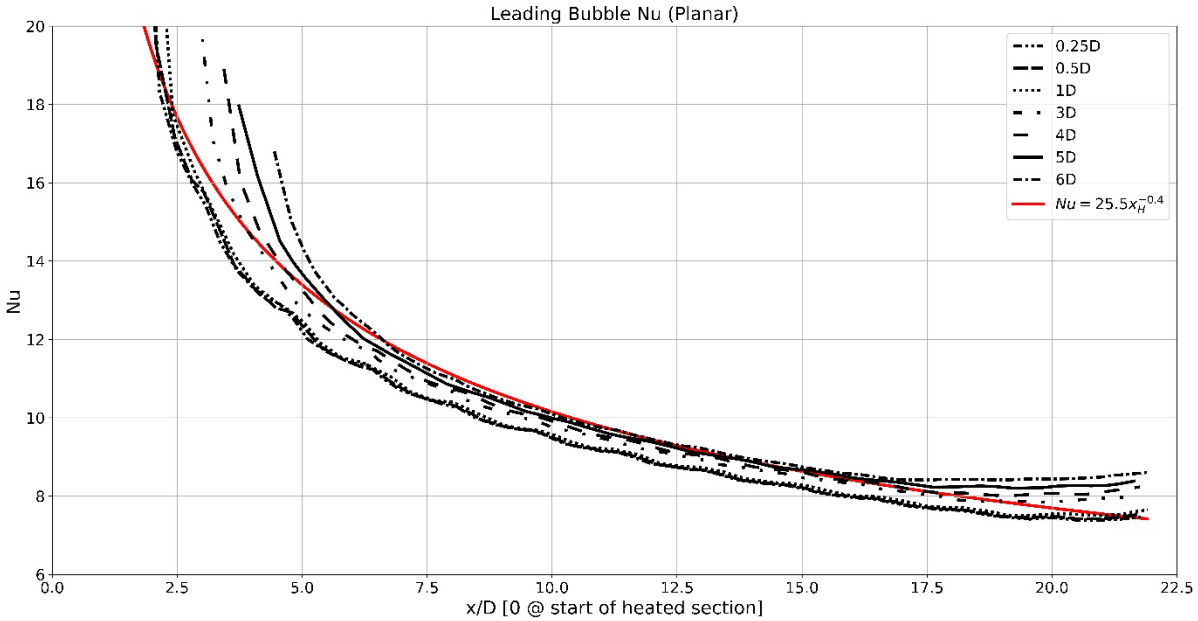

Figure 12: Averaged Nusselt number (Nu) for the leading bubble versus the position of the bubble midpoint, for planar cases.

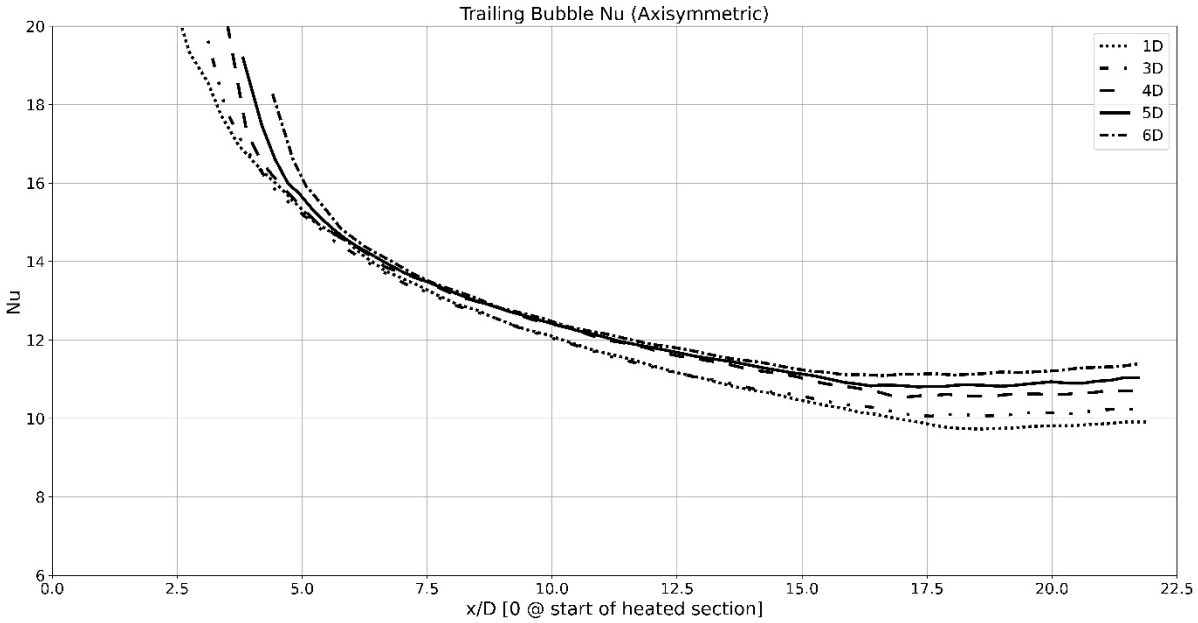

Figure 13: Averaged Nusselt number (Nu) for the trailing bubble versus the position of the bubble midpoint, for axisymmetric cases.

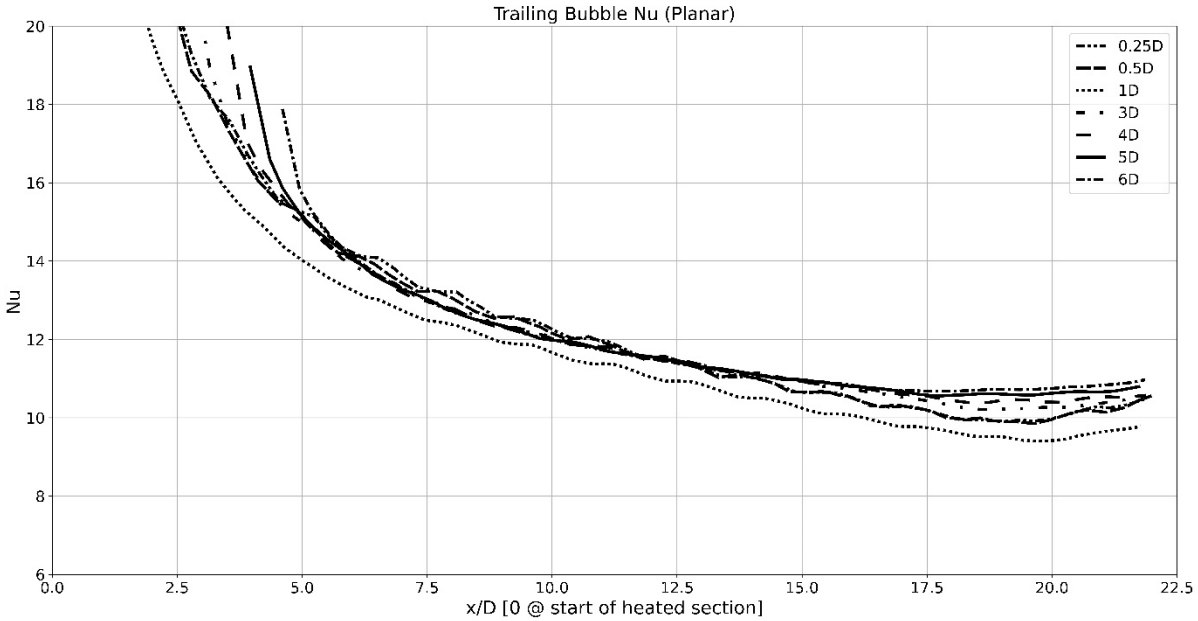

Figure 14: Averaged Nusselt number (Nu) for the trailing bubble versus the position of the bubble midpoint, for planar cases.

The vapour volume was normalised by dividing the volume by the initial vapour volume. The volume increased with time, further illustrating that phase change was present (Figure 15a and Figure 16). When both bubbles are in the heated region, the rate of phase change can be described as linear. This linear behaviour corresponds to eq. 8. Figure 15b illustrates the volume change of the bubbles with time for L_{int} = 3D. The time frames are marked with red dots in Figure 15b.

The average gradients of the change in volume are listed in Table 2 for the interval τ = 20-30. The gradients decreased as the length of the initial spacing was increased, corresponding to Figure 15a and Figure 16. The axisymmetric case of L_{int} = 3D had the highest gradient, although it was not the smallest spacing. This case also had the fastest bubble growth rate for both leading and trailing bubbles. It is not clear why this occurred. This behaviour is not present in the planar cases, suggesting that the geometry might cause this.

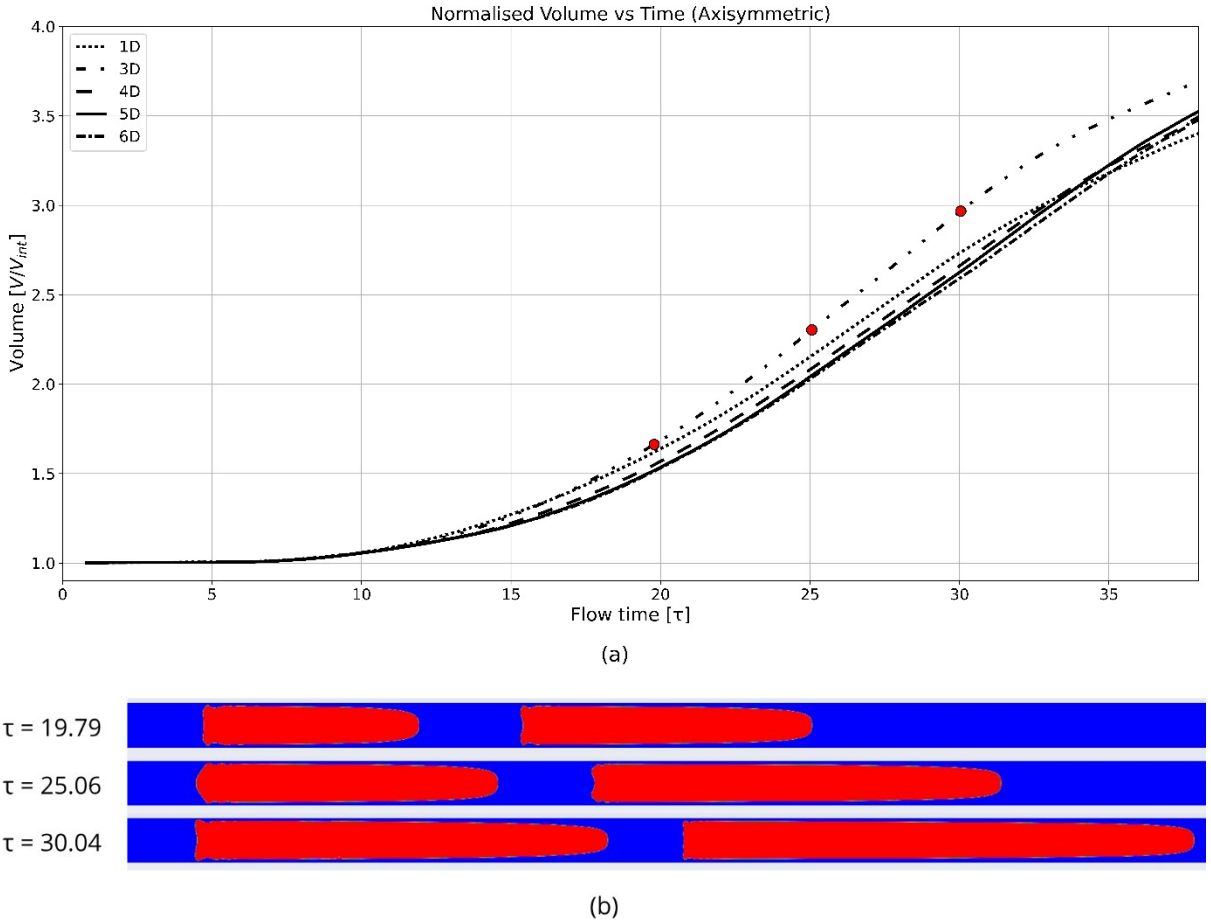

Figure 15: (a) Normalised vapour volume versus time for axisymmetric cases and (b) time frames illustrating volume change with time, corresponding to marked points in (a).

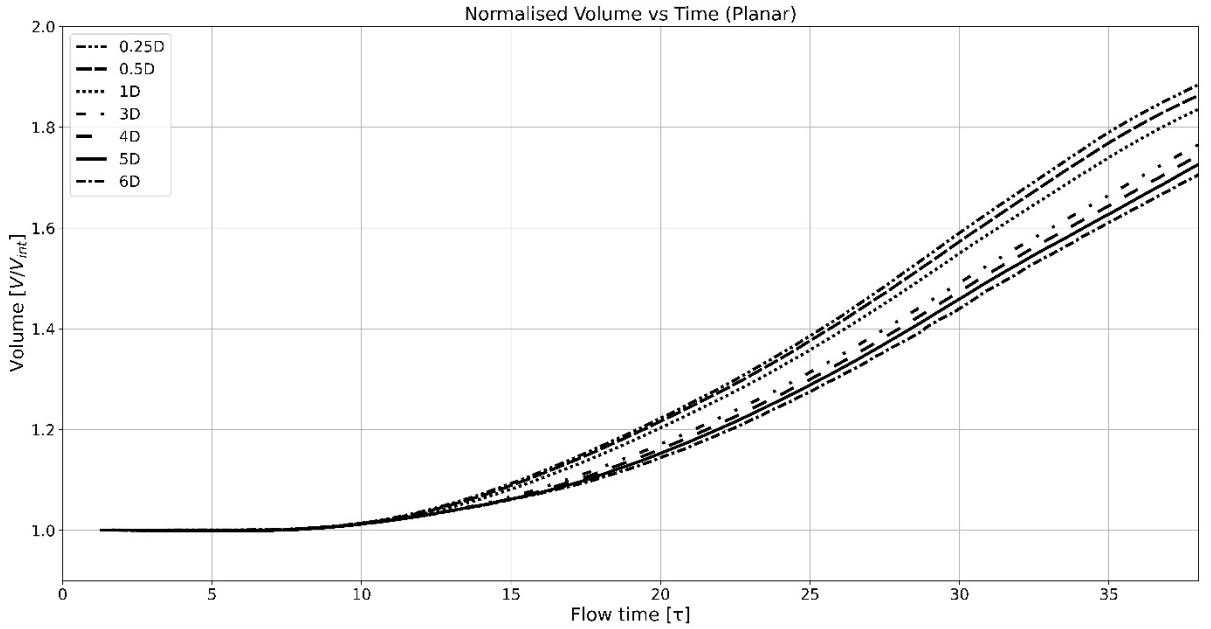

Figure 16: Normalised vapour volume versus time, for planar cases.

Table 2: Average gradient of normalised volume for τ = 20-30 for two-bubble cases.

Initial spacing (L_{int})	Volume gradient for axisymmetric cases	Volume gradient for planar cases
0.25D		0.037
0.5D		0.036
1D	0.110	0.035
3D	0.128	0.032
4D	0.109	0.031
5D	0.109	0.031

4.2 Three-bubble cases

The following initial spacings were used for the three-bubble cases: L_{int} = 0.25D, 0.5D, 1D and 3D. The development of the leading bubble was more varied than for the two-bubble cases (Figure 17). The leading bubble for the L_{int} = 3D case performed similarly in both scenarios, reaching a final length of 6.5D. The other cases all had a shorter final length.

The middle bubble had a more uniform behaviour across the cases with the heat flux present (Figure 18). These bubbles had a final length of between 5 and 5.5D, which was roughly the average length of the trailing bubbles in the two-bubble cases. The growth rate was similar for all the cases with an initial spacing of L_{int} = 1D or less. This uniform behaviour could result from the incompressibility of the liquid slugs between the bubbles and the confinement of the middle bubble.

In contrast to the similarities between the middle bubbles, the trailing bubbles varied significantly (Figure 19). The smaller the initial spacing, the longer the final bubble length. The L_{int} = 0.25D case reached a final length of 6.5D, but the L_{int} = 3D case only reached 4.5D in length.

The middle and trailing bubbles of L_{int} = 3D experienced the same expansion observed for the trailing bubbles of the planar cases in the two-bubble scenario. The equilibrium state is clearly illustrated in Figure 19, as the trailing bubble had to travel further to reach the heated section. Figure 20 and Figure 21 illustrate the middle and trailing bubbles for L_{int} = 0.25D and L_{int} = 3D respectively. The same difference in shape is observed, as shown in Figure 9. The larger spacings allowed for the development of longer and sharper bubbles than the smaller spacing did where the bubbles were confined.

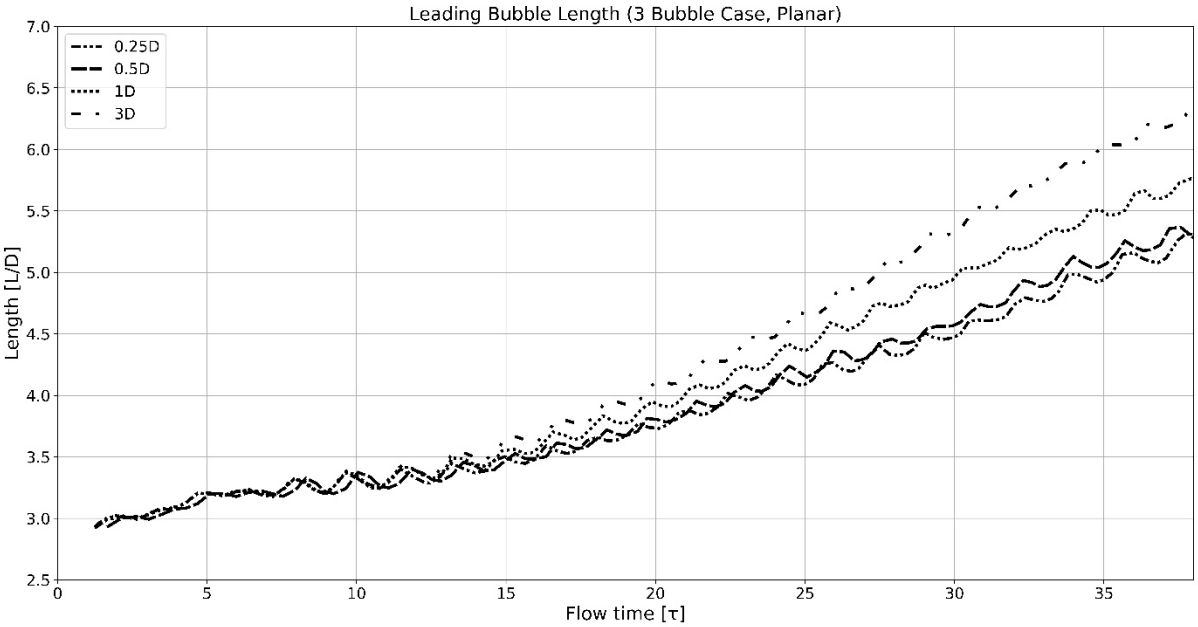

Figure 17: Leading bubble length versus time (three-bubble cases).

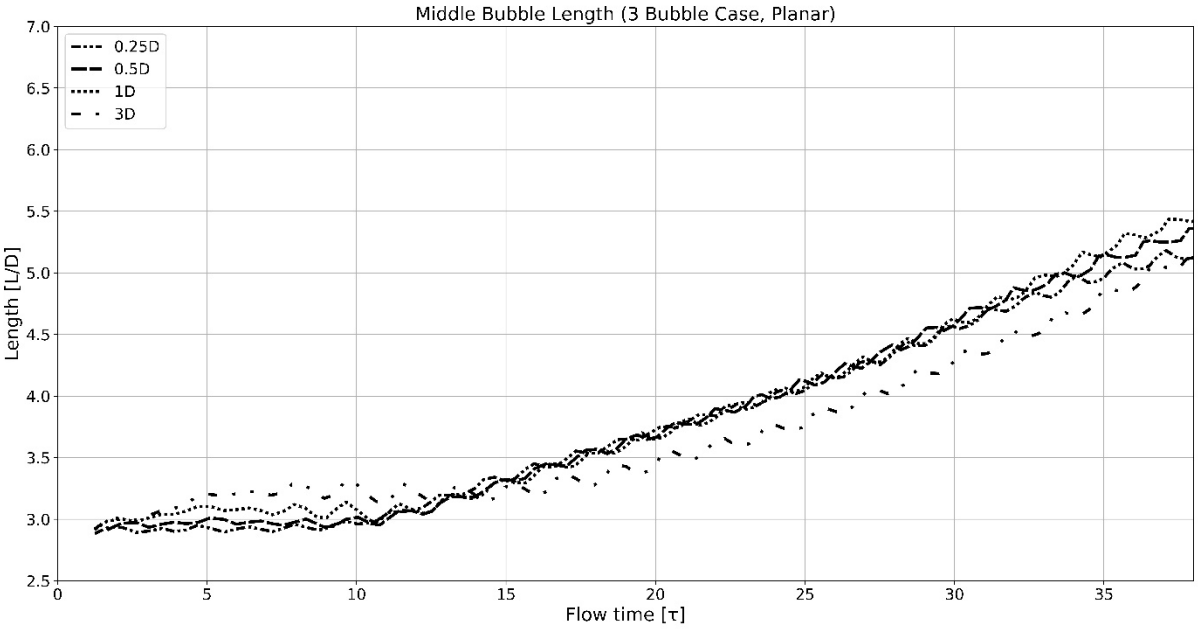

Figure 18: Middle bubble length versus time (three-bubble cases).

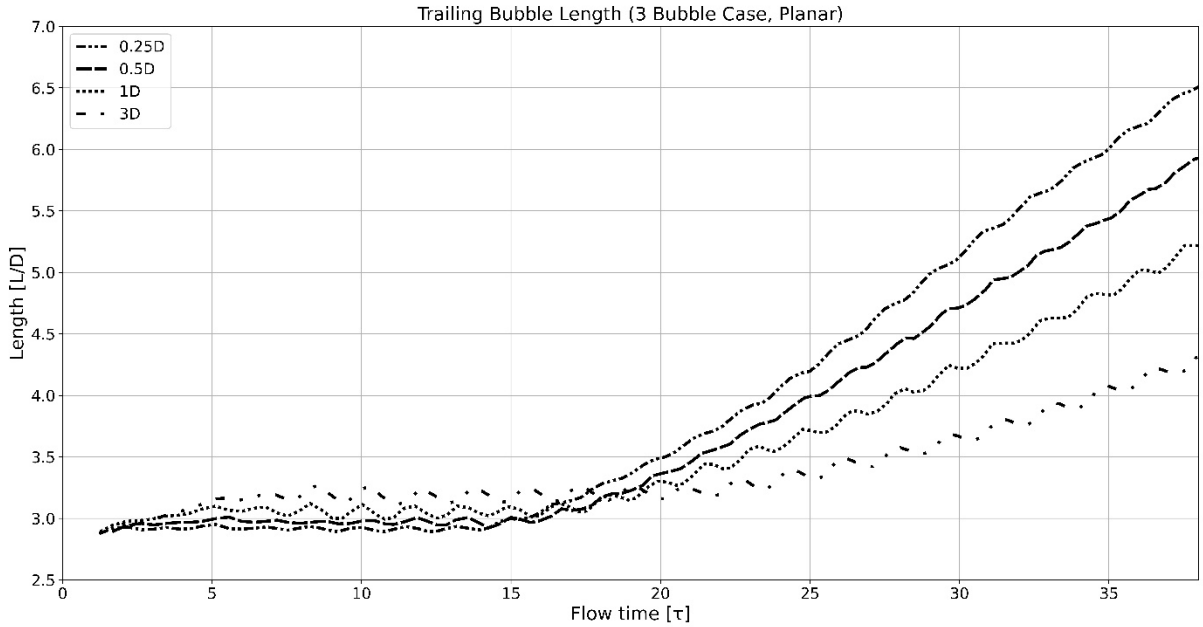

Figure 19: Trailing bubble length versus time (three-bubble cases).

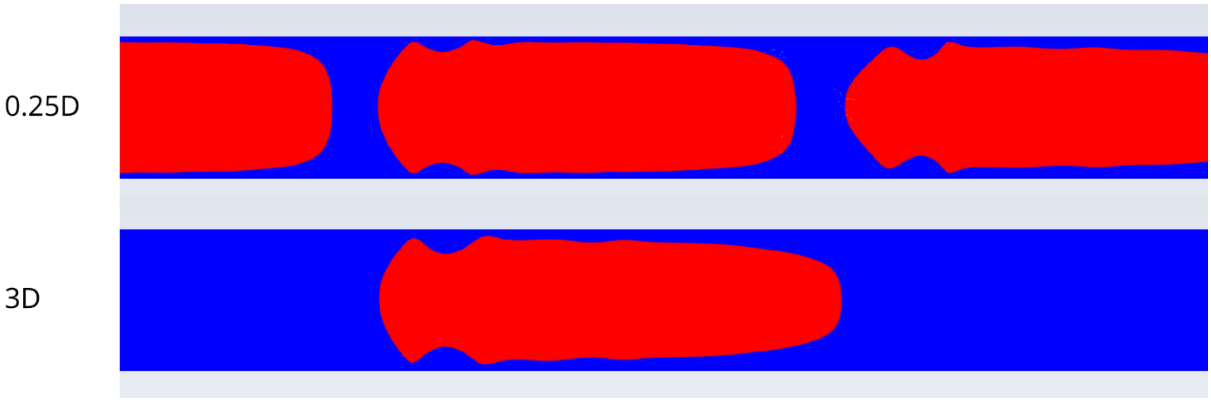

Figure 20: Middle bubbles for Lint = 0.25D and Lint = 3D at τ = 7.9.

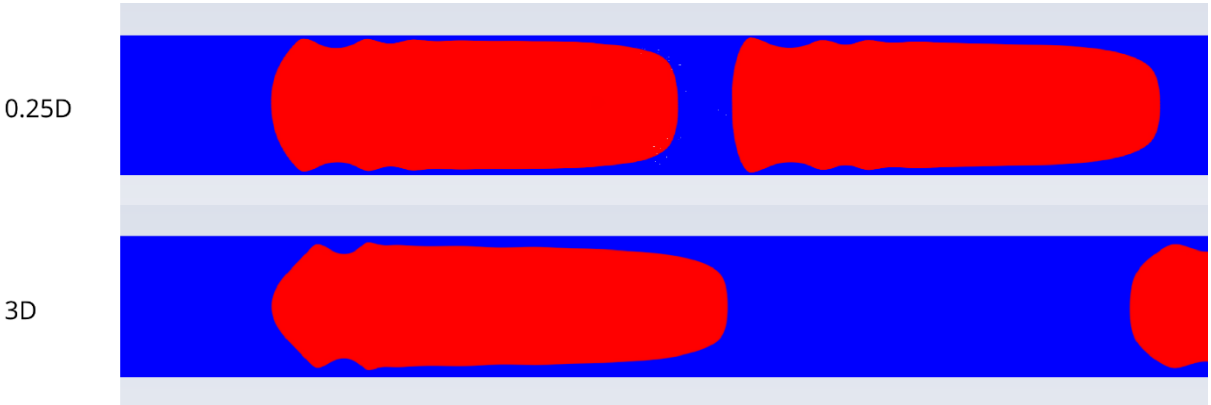

Figure 21: Trailing bubbles for Lint = 0.25D and Lint = 3D at τ = 11.9.

When reviewing the distance between bubbles, a similar trend to the two-bubble scenario is apparent. For the case of L_{int} = 3D, the distance decreased slightly, less than 0.5D, between both the first and second bubble (Figure 22) and the second and third bubble (Figure 23). In the cases where $L_{int} \leq$ 1D, there was a slight increase in the distance between bubbles.

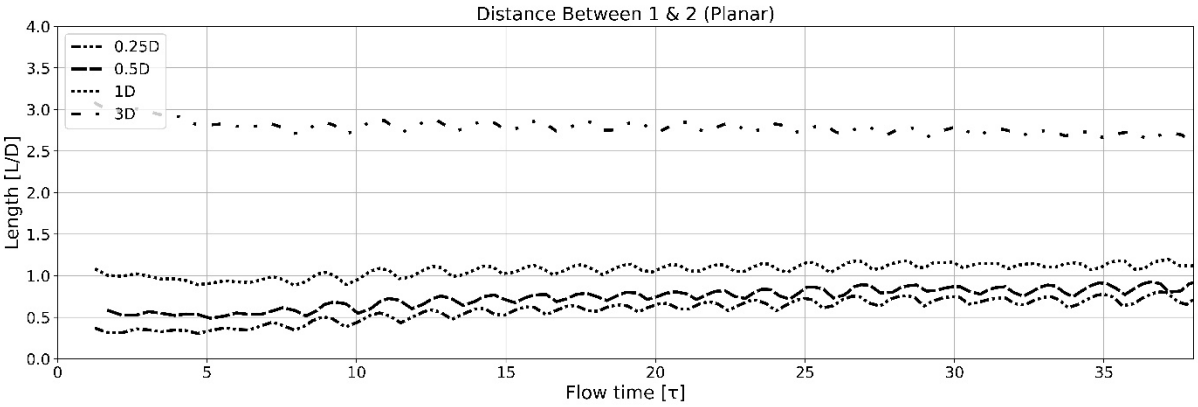

Figure 22: Distance between first and second bubble versus time.

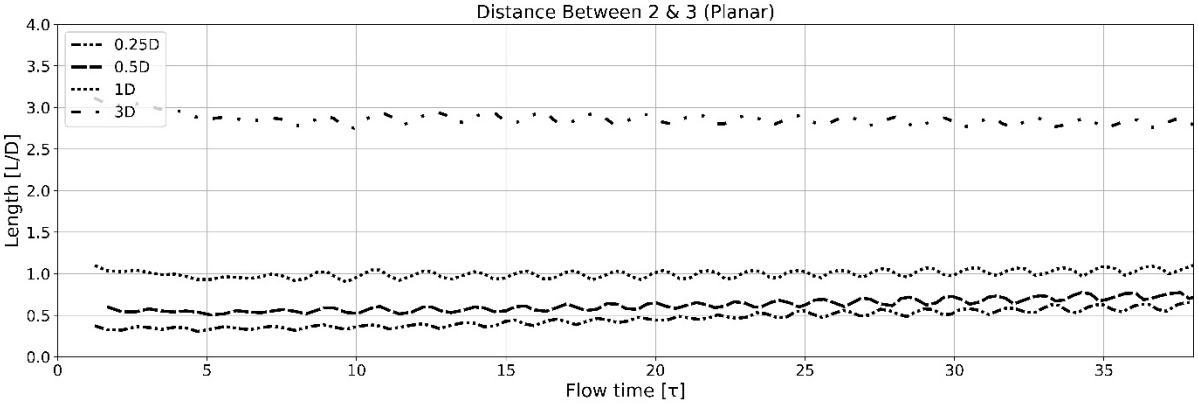

Figure 23: Distance between second and third bubble versus time.

The Nu again improved with each following bubble. The first bubbles had a Nu below 8 when they reached the end of the heated region (Figure 24) and also roughly followed the correlation in eq. 13. The second bubbles had a value between 8 and 10 (Figure 25), and the final bubbles had a value of 12 (Figure 26). This was an increase of 50% over the Nu for the leading bubble. With the first two bubbles, all the cases behaved similarly. While all the cases started off high and reached a similar final value for the last bubble, the gradients differed significantly. The gradients ranged from almost linear for L_{int} = 0.25D to exponential for L_{int} = 3D, resulting in a higher intermediate Nu for the shorter L_{int} cases.

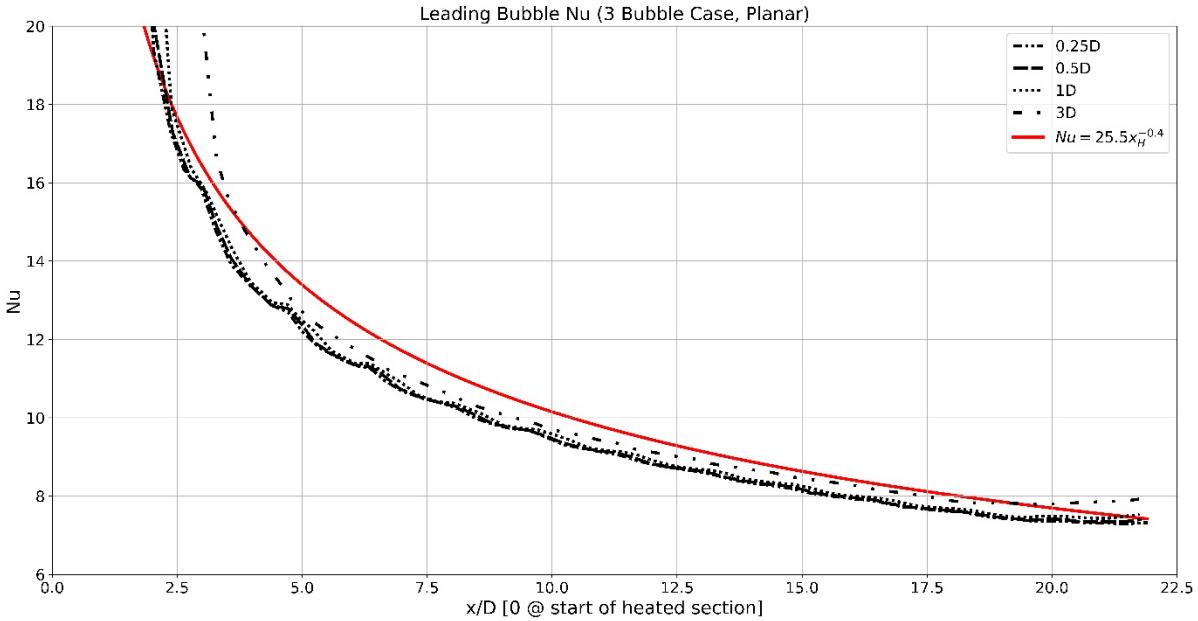

Figure 24: Averaged Nusselt number (Nu) for leading bubble versus bubble midpoint (three-bubble cases).

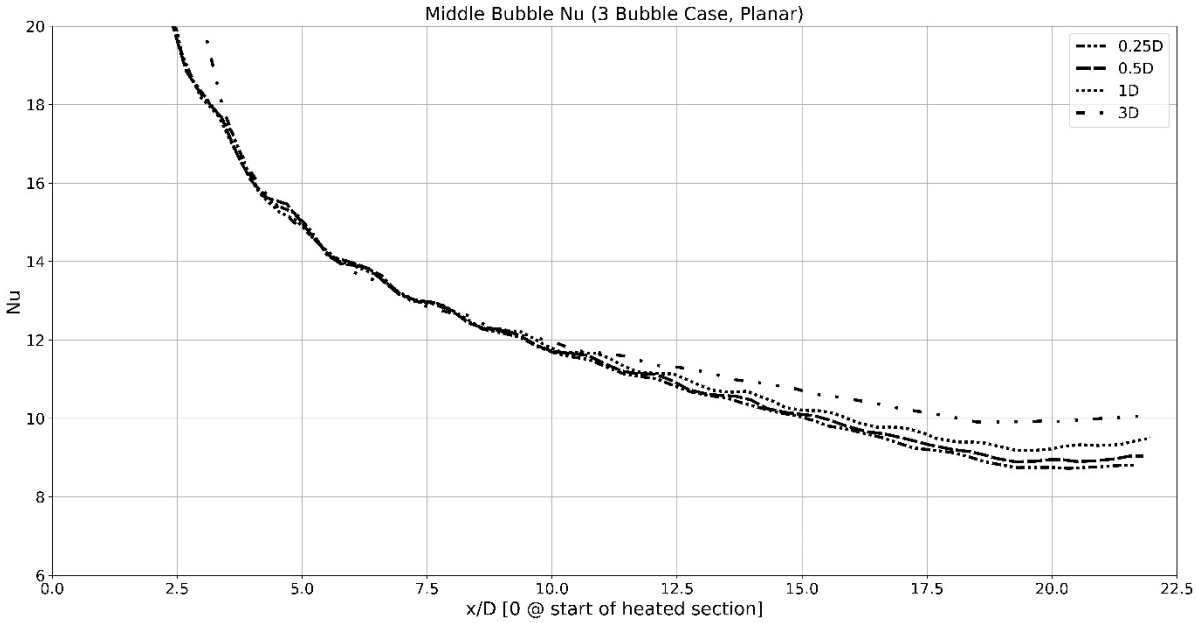

Figure 25: Averaged Nusselt number (Nu) for middle bubble versus bubble midpoint (three-bubble cases).

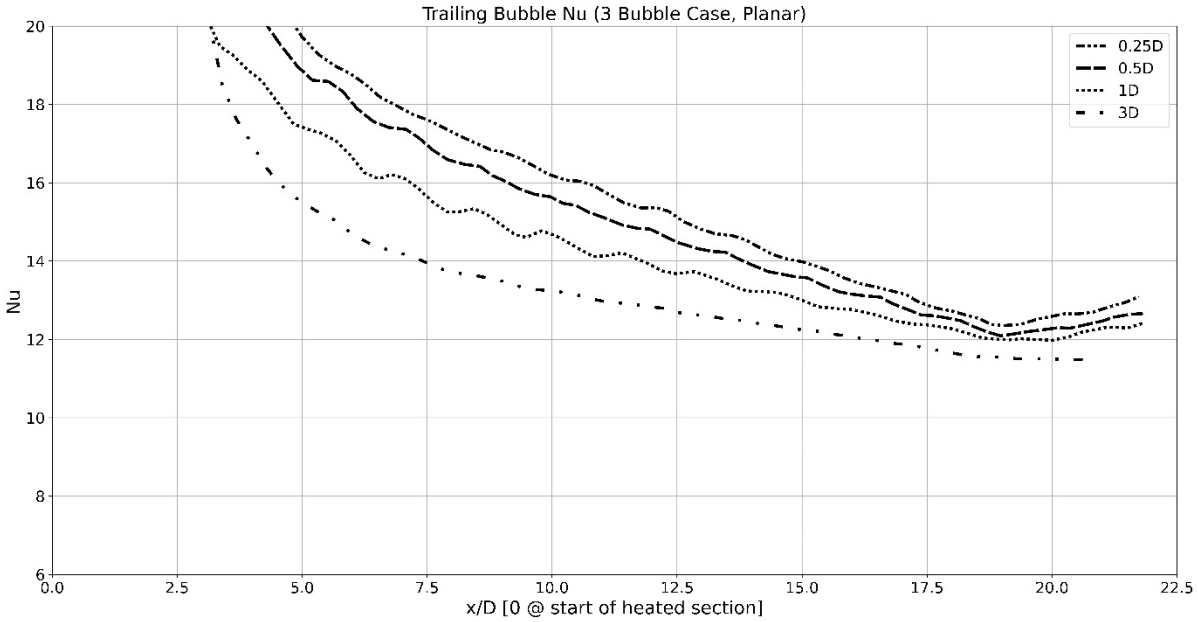

Figure 26: Averaged Nusselt number (Nu) for trailing bubble versus bubble midpoint (three-bubble cases).

Once again, the volume change illustrates a linear-like relation and more mass transfer occurring with a short L_{int}. This is mirrored by the gradients of the volume change listed in Table 3, which show the gradients decreasing as L_{int} increased.

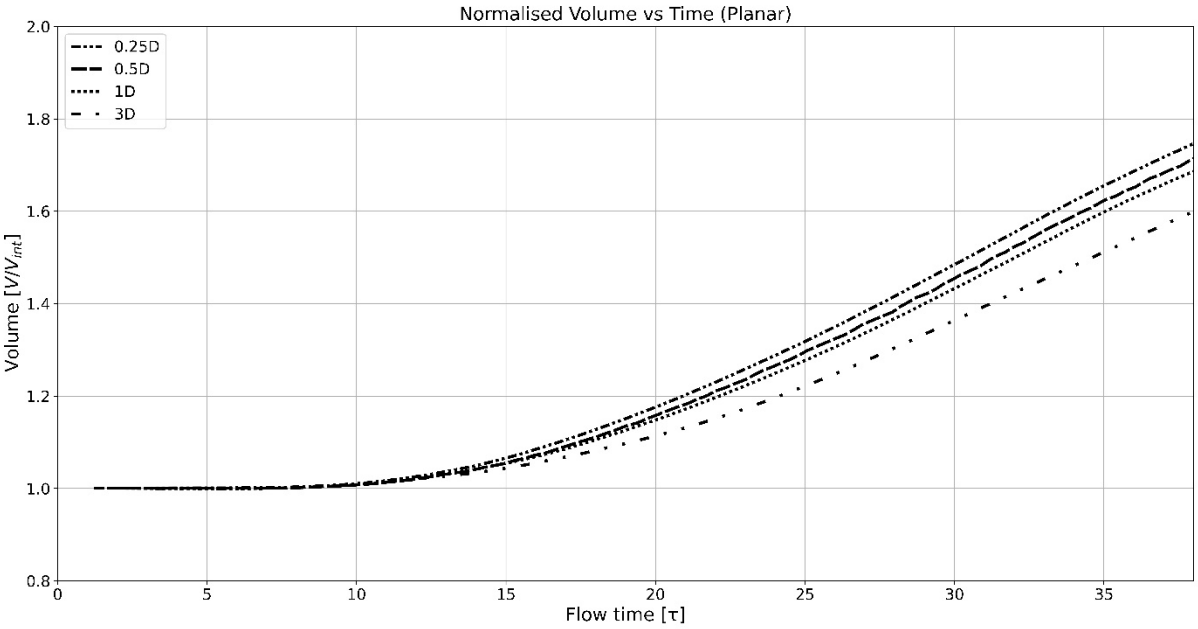

Figure 27: Normalised vapour volume versus time (three-bubble cases).

Table 3: Average gradient of normalised volume for τ = 20-30 for three-bubble cases.

Initial spacing (L_{int})	Volume gradient for three-bubble cases
0.25D	0.0309
0.5D	0.0305
1D	0.0285
3D	0.0252

The case of L_{int} = 0.25D was recreated with a zero-heat flux applied to the heated surface. This case was conducted to ensure that the mass transfer model did not force phase change. The vapour volume remained constant throughout the simulation, proving that phase change was not forced. The velocity of the noses and the tails of the bubbles was calculated from the change in position over time. The difference in velocity at the noses of the leading bubbles was 30%. This decreased towards the tails of the last bubbles, only differing by less than 4%.

4.3 Effects on heat transfer

The following hypothesis can be made from the results above: reducing the distance between bubbles increases the heat transfer. The volume graphs support this hypothesis (Figure 15, Figure 16 and Figure 27). These graphs indicate that the vapour volume increased as the initial spacings were reduced. For all the cases, the Nu increased with sequential bubbles, with a difference between cases becoming more prominent with the trailing bubbles in the three-bubble scenario (Figure 26). This behaviour could be attributed to the time that the thermal boundary layer had to recover. As the bubbles passed, they disturbed the thermal boundary layer. When the bubbles were closer together, less time elapsed before the next bubble moved past the same region. The disturbed boundary layer had a larger temperature difference and thus better heat transfer.

The heat transfer was improved in a couple of ways. Firstly, by the presence of the bubble and the liquid film between the bubble and the channel wall. As the bubble passed, the amount of liquid was reduced and the bubble pushed the thermal boundary layer forward. When the bubble had passed, the boundary layer was still disturbed by the wake of the bubble (Figure 28). Secondly, the recirculation zones replaced the warmer fluid at the wall with cooler fluid from the centre (Figure 29).

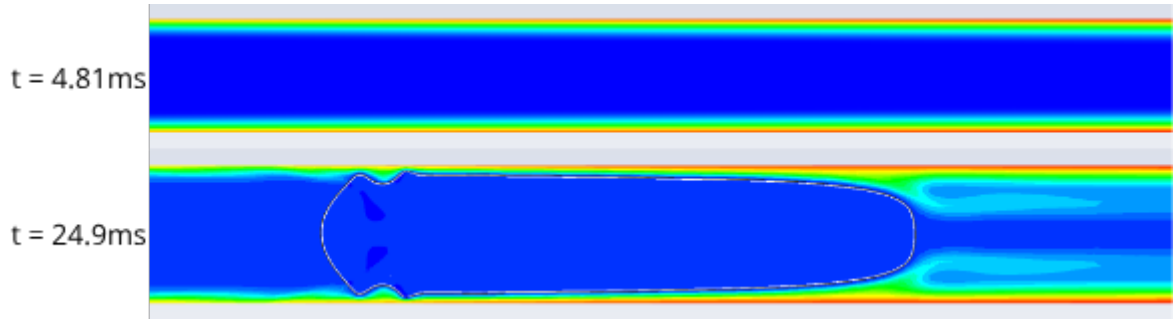

Figure 28: Thermal boundary layer, leading bubble.

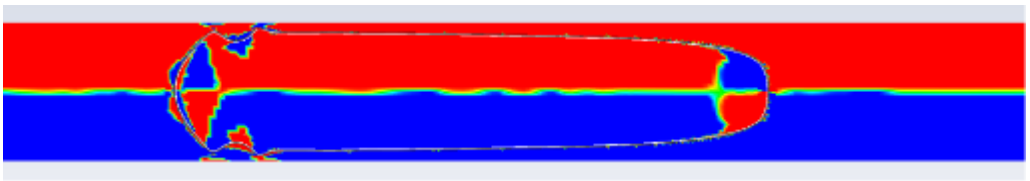

Figure 29: Vorticity. Red is for counterclockwise movement and blue is for clockwise movement.

5. Conclusion

The results above illustrate the value of flow boiling as a cooling method. All the investigated cases showed that the heat transfer coefficient improved in the presence of the vapour bubbles and that sequential bubbles assisted in further improvement, with an increase of 50% observed in the three-bubble scenario. It also became clear that reducing the distance between bubbles led to greater disturbance of the thermal boundary layer. This was illustrated in the larger vapour volumes observed for the smaller initial spacings. Although the trailing bubble in the three-bubble scenario

performed better than the middle bubble, this will not always be the case when more bubbles are present. The heat transfer capabilities will improve with sequential bubbles until a steady state is reached and the bubbles produce a constant Nu.

6. Acknowledgement

The authors gratefully acknowledge the support received from ThermaSMART project of the European Commission (Grant: EC-H2020-RISE-ThermaSMART-778104). The authors also acknowledge the Edinburgh Compute & Data Facility (ECDF) and Centre for High Performance Computing (CHPC), South Africa, for providing computational resources for this research project.

7. References

1. I. Mudawar, Recent advances in high-flux, two-phase thermal management, Journal of Thermal Science and Engineering Applications 5 (2) (2013).
2. A. Sakanova, C.C. Keian and J. Zhao, Performance improvements of microchannel heat sink using wavy channel and nanofluids, International Journal of Heat and Mass Transfer 89 (2015) 59-74.
3. M. Magnini and J. Thome, A CFD study of the parameters influencing heat transfer in microchannel slug flow boiling, International Journal of Thermal Sciences 110 (2016) 119-136.
4. Z. Che, T.N. Wong and N.-T. Nguyen, Heat transfer enhancement by recirculating flow within liquid plugs in microchannels, International Journal of Heat and Mass Transfer 55 (7) (2012) 1947-1956.
5. Y. Sui, C. Teo, P.S. Lee, Y. Chew and C. Shu, Fluid flow and heat transfer in wavy microchannels, International Journal of Heat and Mass Transfer 53 (13-14) (2010) 2760-2772.
6. P. Naphon, Laminar convective heat transfer and pressure drop in the corrugated channels, International Communications in Heat and Mass Transfer 34 (1) (2007) 62-71.
7. Y.A. Çengel and A.J. Ghajar, Heat and Mass Transfer: Fundamentals & Applications. 5th edition, McGraw Hill Education, New York, 2015, pp. 596-611.
8. E. Chinnov, F. Ronshin and O. Kabov, Features of two-phase flow in a rectangular microchannel with the height of 300 μm, Thermophysics and Aeromechanics 21 (2015) 759-762.
9. M. Magnini, B. Pulvirenti and J. Thome, Numerical investigation of the influence of leading and sequential bubbles on slug flow boiling within a microchannel, International Journal of Thermal Sciences 71 (2013) 36-52.
10. A. Bordbar, A. Taassob, A. Zarnaghsh and R. Kamali, Slug flow in microchannels: Numerical simulation and applications, Journal of industrial and engineering chemistry 62 (2018) 26-39.
11. D. Mikaelian, B. Haut and B. Scheid, Bubbly flow and gas–liquid mass transfer in square and circular microchannels for stress-free and rigid interfaces: dissolution model, Microfluidics and Nanofluidics 19 (2015) 899-911.
12. A. Ferrari, M. Magnini and J.R. Thome, Numerical analysis of slug flow boiling in square microchannels, International Journal of Heat and Mass Transfer 123 (2018) 928-944.
13. A.M. Jacobi and J.R. Thome, Heat transfer model for evaporation of elongated bubble flows in microchannels, Journal of Heat Transfer 124 (6) (2002) 1131-1136.
14. J. Thome, V. Dupont and A.M. Jacobi, Heat transfer model for evaporation in microchannels. Part I: presentation of the model, International Journal of Heat and Mass Transfer 47 (14-16) (2004) 3375-3385.
15. A. Abdollahi, R.N. Sharma and A. Vatani, Fluid flow and heat transfer of liquid-liquid two phase flow in microchannels: A review, International Communications in Heat and Mass Transfer 84 (2017) 66-74.

16. S. Szczukiewicz, M. Magnini and J.R. Thome, Proposed models, ongoing experiments, and latest numerical simulations of microchannel two-phase flow boiling, International journal of multiphase flow 59 (2014) 84-101.
17. R. Courant, K. Friedrichs and H. Lewy, On the partial difference equations of mathematical physics, IBM journal of Research and Development 11 (2) (1967) 215-234.
18. J. Potgieter, Numerical investigation on the effect of gravitational orientation on bubble growth during flow boiling in a high aspect ratio microchannel, Master thesis, University of Pretoria, Pretoria, 2019.
19. I. Tanasawa, Advances in Condensation Heat Transfer. in: J.P. Hartnett, T.F. Irvine, and Y.I. Cho, eds, Advances in Heat Transfer, Elsevier, Tokyo, 1991, pp. 55-139.
20. M. Vermaak, J. Potgieter, J. Dirker, M.A. Moghimi, P. Valluri, K. Sefiane, and J.P. Meyer, Experimental and numerical investigation of micro/mini channel flow-boiling heat transfer with non-uniform circumferential heat fluxes at different rotational orientations, International Journal of Heat and Mass Transfer 158 (2020) 119948.